catalysts

MDPI

*Article*

# Visible-Light-Driven GO/Rh-$SrTiO_3$ Photocatalyst for Efficient Overall Water Splitting

**Shuai Zhang [1], Enhui Jiang [2], Ji Wu [1], Zhonghuan Liu [1], Yan Yan [1], Pengwei Huo [1,*] and Yongsheng Yan [1,*]**

[1] School of Chemistry and Chemical Engineering, Jiangsu University, Zhenjiang 212013, China
[2] School of Materials Science and Engineering, Jiangsu University, Zhenjiang 212013, China
* Correspondence: huopw@ujs.edu.cn (P.H.); yys@ujs.edu.cn (Y.Y.)

**Abstract:** The combining of the heterostructure construction and active sites modification to remodel the traditional wide-band-gap semiconductor $SrTiO_3$ for improving visible light absorption capacity and enhancing photocatalytic performance is greatly desired. Herein, we research a novel GO/Rh-$SrTiO_3$ nanocomposite via a facile hydrothermal method. The champion GO/Rh-$SrTiO_3$ nanocomposite exhibits the superior photocatalytic overall water splitting performance with an $H_2$ evolution rate of 55.83 $\mu mol \cdot g^{-1} \cdot h^{-1}$ and $O_2$ production rate of 23.26 $\mu mol \cdot g^{-1} \cdot h^{-1}$, realizing a breakthrough from zero with respect to the single-phased STO under visible light ($\lambda \geq 420$ nm). More importantly, a series of characterizations results showed that significantly improving photocatalytic performance originated mainly from the construction of heterostructure and more active sites rooted in Rh metal. In addition, the possible photocatalytic reaction mechanisms and the transport behavior of photogenerated carriers have been revealed in deeper detail. This work provides an effective strategy for heterostructure construction to improve solar utilization through vastly expanding visible light response ranges from traditional UV photocatalysts.

**Keywords:** $SrTiO_3$; GO; Rh active sites modification; photocatalytic overall water splitting; energy conversion



**Citation:** Zhang, S.; Jiang, E.; Wu, J.; Liu, Z.; Yan, Y.; Huo, P.; Yan, Y. Visible-Light-Driven GO/Rh-$SrTiO_3$ Photocatalyst for Efficient Overall Water Splitting. *Catalysts* **2023**, *13*, 851. https://doi.org/10.3390/catal13050851

Academic Editor: Jae Sung Lee

Received: 28 March 2023
Revised: 2 May 2023
Accepted: 3 May 2023
Published: 8 May 2023



## 1. Introduction

The excessive consumption of fossil energy has led to serious energy and environmental problems [1] while promoting the research of green alternative energy sources [2]. Hydrogen is considered to be an optimal clean energy source because of its low density, high calorific value, easy storage, and non-toxicity [3]. At the same time, its combustion product is only water, which effectively avoids greenhouse gas emissions, so achieving efficient, clean, and low-energy hydrogen production is significant in the current development. Unlike fossil fuels, hydrogen is not readily available directly in nature. Fortunately, hydrogen can be produced from primary energy sources such as coal, crude oil, natural gas, biomass, and solar energy. Many process technologies for hydrogen production have been developed, such as pyrolysis, fermentation, electrocatalysis, and photocatalysis [4]. Currently, the largest hydrogen production comes from coal gasification, methane steam reforming, and methane partial oxidation technologies [5]. However, the excessive depletion of fossil fuels and significant environmental issues have promoted the development of viable alternatives. Among them, photocatalytic water splitting, which uses solar energy and water, is a promising option [6]. In recent years, photocatalytic technology has received widespread attention because of its clean, safe, sustainable, and longevous advantages. In the photocatalytic system, a decisive role in the overall water splitting efficiency is played by the photocatalyst, which is the core of the whole system [7,8]. It is well known that suitable band structure, abundant reactive sites, and efficient photogenerated carrier separation are the criteria for excellent photocatalysts [9,10]. However, there are very few photocatalysts that can meet these criteria. Therefore, it is essential to study an efficient photocatalyst.

In recent years, $SrTiO_3$ (abbreviated as STO) has been widely used in photocatalysis [11], sensors [12], dye-sensitized solar cells (DSCC) [13], and supercapacitors [14] because of its excellent properties, including high dielectric constant, resistance to photochemical corrosion, relatively stable properties, and non-toxicity [15,16]. Nevertheless, the excessively wide energy band (~3.2 eV) of STO semiconductors leads to poor photogenerated electron–hole pair separation and low utilization of visible light, which results in poor photocatalytic performance [17]. Therefore, improving the visible light utilization of STO is a major challenge. Currently, the modification of photocatalysts involves heterostructure construction [18,19], defect generation [20,21], elemental doping [22,23], and active sites modification [24,25]. Ha's group synthesized $SrTiO_3/TiO_2$ heterostructures with different morphologies by a simple hydrothermal method. The $SrTiO_3/TiO_2$ heterostructures not only facilitate the rapid separation of photogenerated electron–hole pairs but also allow more light absorption, which has a synergistic effect that enhances the photocatalytic activity of $SrTiO_3/TiO_2$ heterostructures [26]. Deng's group synthesized $SrTiO_3$-$SrCO_3$ heterostructures by a simple hydrothermal method. The $SrTiO_3$-$SrCO_3$ heterostructures facilitate the rapid separation and transmission of photogenerated carriers. Under simulated sunlight irradiation, the champion $SrTiO_3$-$SrCO_3$ showed a great photocatalytic $H_2$ production rate of 4.73 $mmol \cdot h^{-1} \cdot g^{-1}$, which was 21 times higher than that of pure $SrTiO_3$ [27]. The strategy of constructing heterostructures was applied to STO and other semiconductors, significantly improving the utilization of visible light and the separation and migration of charge carriers [28].

Graphene oxide (GO) is widely used for the synthesis of efficient photocatalysts because of its big specific surface area, outstanding electrical conductivity, and powerful light absorption ability [29,30]. For example, Jung's group combined GO with $TiO_2$ and ZnO to increase light utilization and reduce electron–hole pairs recombination in the composite [31]. Gao's group synthesized GO/CdS composites by a novel two-phase hybrid method. The efficient electron transfer from CdS to GO decreased the recombination of photogenerated carriers which improved the catalytic activity [32]. Hunge's group has synthesized $GO/TiO_2$ composite using a hydrothermal process. A series of characterizations showed that the occurrence of GO not only accelerates electron transfer and thus inhibits the recombination of photogenerated electron–hole pairs but also increased light absorption and utilization, which improved the photocatalytic activity [33]. Herein, GO was applied to improve STO light utilization and conductivity. Meanwhile, the active sites are also important for overall water splitting, and metal elements are usually chosen as the electron acceptor and as the active sites for the reaction. For example, Cai's group successfully constructed metal/phosphide heterostructures by photo-deposition which drove a dual active site mechanism thereby overcoming the low efficiency of precious metal water splitting and providing an effective strategy for the preparation of high performance water splitting catalysts [34]. The use of the Rh metal as the electron acceptors greatly increases the exposed active sites and promotes the electron–hole separation.

In this work, heterostructure construction and active site modification strategies have been applied to fabricate GO/Rh-STO composites by a hydrothermal process. Notably, the prepared GO/Rh-STO composites show excellent photocatalytic overall water splitting performance under visible light. In addition, the influencing factors to enhance the photocatalytic activity and the rational photocatalytic reaction mechanism were also investigated in depth. This study combines heterostructure construction techniques (GO improved light absorption) and active sites modification (Rh metal increased active sites) to improve photocatalytic overall water splitting performance, which provides a new strategy to transform traditional UV catalysts into visible-light-responsive catalysts with abundant active sites applied to energy conversion.

## 2. Results and Discussions

### *2.1. Characterization of GO/Rh-STO Photocatalysts*

The microstructure and morphological characteristics of the prepared catalysts were analyzed by SEM, TEM, HRTEM, and EDS mapping. Figure 1a,d show the SEM and TEM images of STO which show a smooth surface of hexagonal nanosheets without any other impurities, thereby confirming the formation of STO nanosheets. Figure 1b shows the SEM image of GO with a large specific surface area, clearly illustrating the disorderly stacked, and folded sheet-like accumulation. Figure 1c,e show SEM and TEM images of GO/Rh-STO heterostructures, showing that STO nanoparticles grown on the GO flakes. In Figure 1f, the HRTEM image of the GO/Rh-STO heterostructure shows the heterostructure interface between GO and STO, thereby confirming the formation of the GO/Rh-STO heterostructure. Moreover, the clean lattice spacing of 0.224 nm matches well with the (111) plane of STO, while GO is amorphous with no clear lattice. In addition, Figure 1g shows the HAADF and EDS mapping images which show all elements of Sr, Ti, O, Rh, and C in the GO/Rh-STO composite catalysts, which further confirms the formation of GO/Rh-STO composite catalysts. The above results confirm the formation of GO/Rh-STO heterostructures.

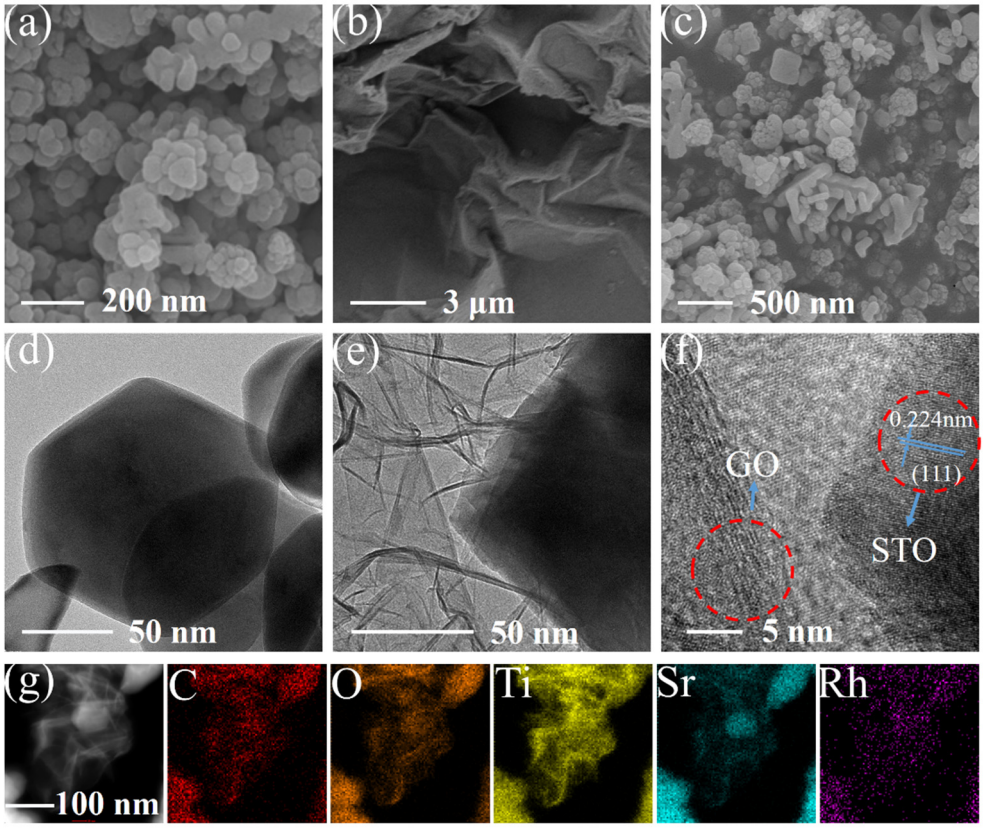


**Figure 1.** SEM images of (**a**) STO, (**b**) GO and (**c**) GO/Rh-STO; (**d**) TEM image of STO, (**e**) TEM, (**f**) HRTEM, (**g**) HADDF and EDS mapping images of GO/Rh-STO.

### *2.2. The Crystal Structure and Chemical States Analysis*

To better understand the structure and chemical state of pure STO and GO/Rh-STO, XRD patterns and XPS analysis were investigated. As shown in Figure 2a, the STO nanosheets show good crystallinity with diffraction peaks at 22.75°, 32.40°, 39.96°, 46.47°, 52.35°, 57.76°, and 67.83°, which corresponds to (100), (110), (111), (200), (012), (211), and (220) crystal planes of the STO structure, respectively. These peaks are characteristic peaks of STO, indexing to JCPDS card number 35-0734 [35]. The STO crystalline structure is well-developed based on the well-defined and very sharp peaks in the XRD patterns of the STO nanosheets. As shown in Figure 2b, the XRD pattern of GO shows an intense and sharp

peak at 2θ = 10.40° that correspond to the (001) plane of GO, which is usually determined by the synthesis process and the number of water layers in the interplanar space of GO [36,37]. The XRD patterns of GO/Rh-STO nanocomposites clearly show GO and STO characteristic diffraction peaks, which proves the presence of GO and STO in the nanocomposites, while the decrease of GO characteristic peak intensity indicates that the aggregation of GO sheets has been greatly decreased. Therefore, the XRD patterns confirmed the successful synthesis of GO, STO, and GO/Rh-STO nanocomposites. Figure 3a shows that there are Ti, Sr, Rh, C, and O elements in GO/Rh-STO. As shown in Figure 3b, two symmetric diffraction peaks (309.4 eV and 314.4 eV) appeared in the Rh 3d XPS spectrum which corresponded to Rh 3d $_{5/2}$ and 3d $_{3/2}$, representing $Rh^{4+}$ rather than $Rh^{3+}$ or the oxide form of Rh [38,39]. This suggests that Rh is successfully modified into the STO lattice by substitution at the Ti position. Figure 3c shows the XPS patterns of O elements in GO and GO/Rh-STO samples. The diffraction peak of lattice oxygen in GO/Rh-STO sample shifts from 529.8 eV to lower binding energy, which is due to the interference generated by Rh atoms entering the STO crystal structure, and further confirms the successful modification of Rh in STO. The XPS spectra of Ti 2p and Sr 3d of STO and GO/Rh-STO are shown in Figure 3d,e, respectively, which show that the integration of Rh metal active sites modification and GO heterostructure construction in the STO nanosheets does not change the XPS of Ti 2p and Sr 3d too much. This result suggests that the incorporation of GO and the Rh metal does not change the core structure of STO.

The XPS atomic percentage analysis of xGO/Rh-STO as shown in Table 1. The percentages of C atomic were 3.8%, 7.2%, 12.2%, and 16.9%, respectively, and named 3.8% GO/Rh-STO, 7.2% GO/Rh-STO, 12.2% GO/Rh-STO, and 16.9% GO/Rh-STO, according to the atomic percentage analysis of XPS.

**Table 1.** The XPS atomic percentage analysis of xGO/Rh-STO.

| GO Addition Amount (mg) | Atomic %C | Atomic %O | Atomic %Rh | Atomic %Sr | Atomic %Ti |
|---|---|---|---|---|---|
| 10 | 3.8 | 53.9 | 0.7 | 25.1 | 16.5 |
| 20 | 7.2 | 53.7 | 0.6 | 23.1 | 15.4 |
| 40 | 12.2 | 51.4 | 0.5 | 21.7 | 14.2 |
| 60 | 16.9 | 48.1 | 0.4 | 18.4 | 12.5 |

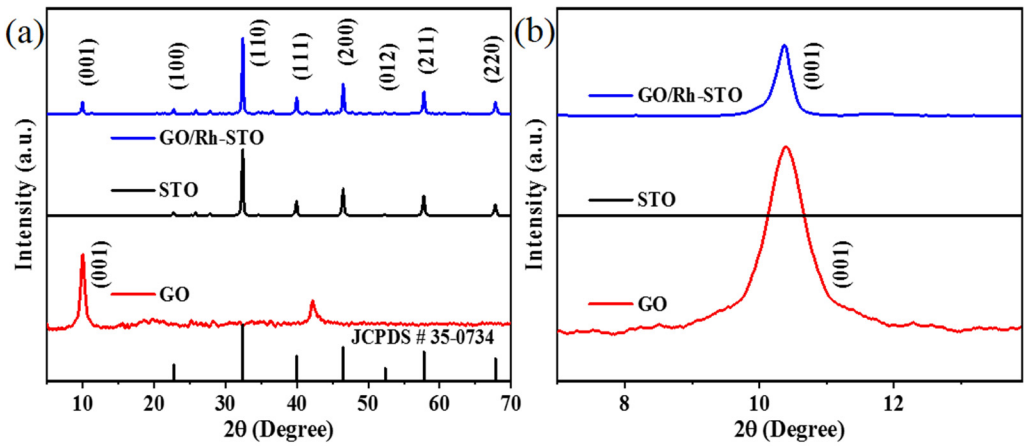


**Figure 2.** (**a**,**b**) XRD patterns of the GO, STO, and GO/Rh-STO.

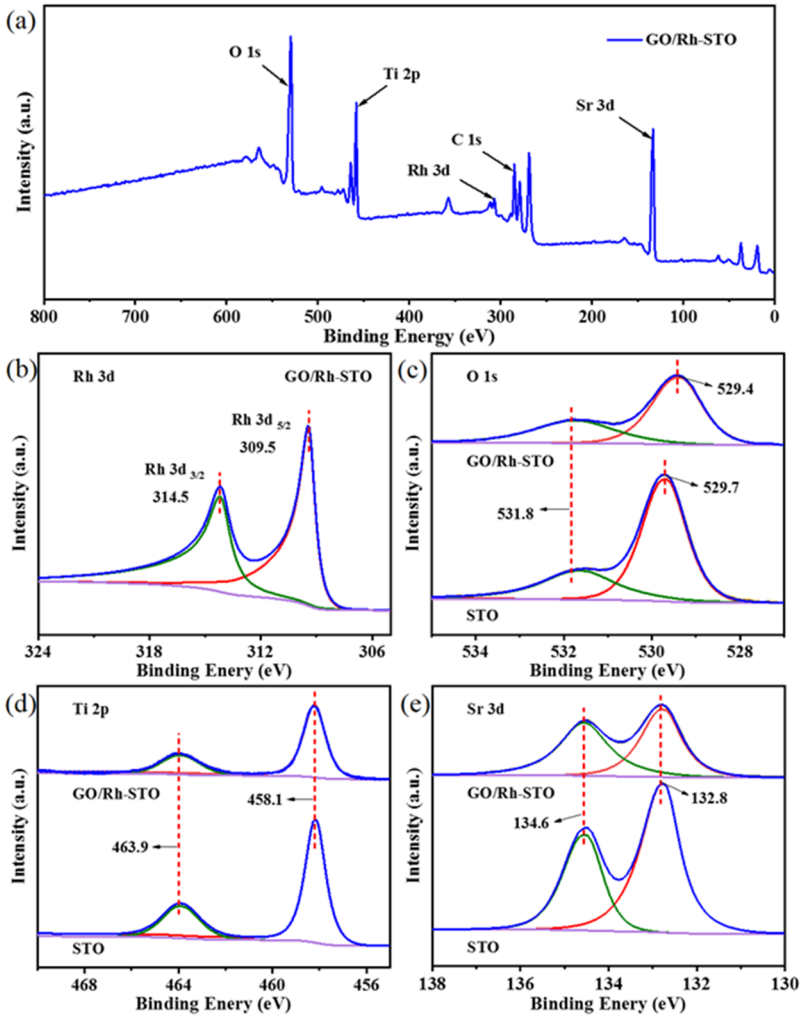


**Figure 3.** XPS spectra of STO and GO/Rh-STO: (**a**) the total survey spectra, (**b**) Rh 3d, (**c**) O 1s, (**d**) Ti 2p, (**e**) Sr 3d.

### *2.3. Photocatalytic Performance Evaluation*

The photocatalytic performance of the prepared photocatalysts was investigated by overall water splitting for $H_2$ and $O_2$ production. As shown in Figure 4a, pure STO cannot overall water splitting under visible light ($\lambda \geq 420$ nm) due to the fact that it can only absorb and utilize UV light. However, the overall water splitting of GO/STO heterostructure can work under visible light. The champion GO/Rh-$SrTiO_3$ nanocomposite exhibits the superior photocatalytic overall water splitting performance with an $H_2$ evolution rate of 55.83 $\mu mol \cdot g^{-1} \cdot h^{-1}$ and $O_2$ production rate of 23.26 $\mu mol \cdot g^{-1} \cdot h^{-1}$ under visible light ($\lambda \geq 420$ nm), illustrating that the heterostructure construction and Rh metal active sites modification enhanced the utilization of visible light and photocatalytic performance of STO. As shown in Figure 4b, the $H_2$ and $O_2$ production rates over the xGO/Rh-STO samples are increased and then decreased with the increasing amount of GO, the possible reason for which can be ascribed to the fact that the excess GO reduces the exposed active sites of STO, resulting in a reduction in the overall water splitting rate. Notably, the 7.2% GO/Rh-STO photocatalyst displays the highest $H_2$ production rate (55.83 $\mu mol \cdot g^{-1} \cdot h^{-1}$) and $O_2$ production rate (23.26 $\mu mol \cdot g^{-1} \cdot h^{-1}$) under visible light ($\lambda \geq 420$ nm).

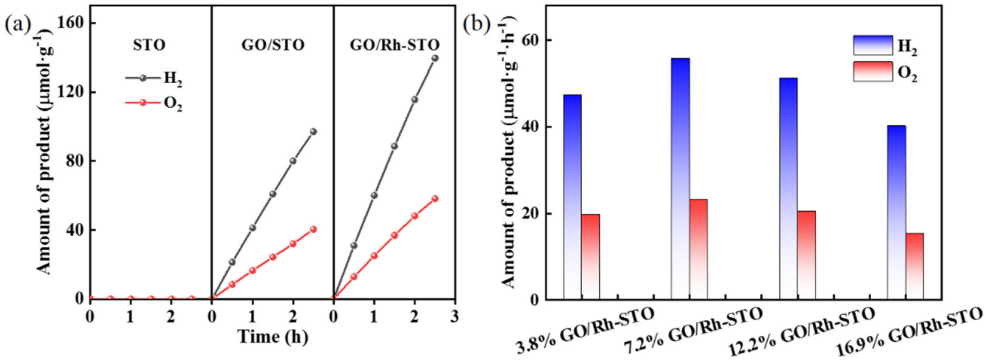


**Figure 4.** (**a**) Time course of $H_2$ and $O_2$ evolution over STO, GO/STO, GO/Rh−STO, and (**b**) photocatalytic activity of xGO/Rh−STO (x = 3.8%, 7.2%, 12.2%, or 16.9%) under visible light (λ ≥ 420 nm) irradiation.

In recent years, there have been many works aimed at enhancing the performance of STO overall water splitting as shown in Table 2. Modulating the morphology of STO is also an effective strategy to improve photocatalytic activity, in addition to the forming of composite materials. Many different morphological STO samples have been reported, such as nanoparticles, nanosheets, nanospheres, nanorods, coral-like and flower-like microspheres, etc. [40–43] The study of STO with different morphologies revealed that highly interconnected porous structures are more favorable for reactant adsorption, light utilization, and carrier migration. For example, flower-like STO with a large number of cavities facilitates a reduction in photogenerated carrier recombination while facilitating the reflection of light to improve light utilization [42,43]. These are the keys to improving the photocatalytic activity of STO. Morphological modulation provides a strategy to further improve the photocatalytic activity of GO/Rh-STO. The modified STO catalysts showed relatively high overall water splitting performance under UV light and low performance under visible light. This work synthesized GO/Rh-STO photocatalyst and exhibited excellent overall water splitting performance compared to other works under visible light. The GO/Rh-STO composites have great potential for large-scale photocatalytic overall water splitting applications, but their performance at present is still insufficient and much work needs to be carried out to improve the overall water splitting performance of GO/Rh-STO under visible light.

**Table 2.** The comparison of overall water splitting performance of STO-based photocatalysts in other works.

| Materials | Catalyst Dosage (mg) | Cocatalysts | Reactant Solution Water (mL) | Light Source | $H_2$ Rate ($\mu molh^{-1} \cdot g^{-1}$) | $O_2$ Rate ($\mu molh^{-1} \cdot g^{-1}$) | Ref. |
|---|---|---|---|---|---|---|---|
| GO/Rh-STO | 100 | / | 100 | 300W Xe Lamp (λ > 420 nm) | 55.83 | 23.26 | This work |
| $SrTiO_3$-C950 | 400 | / | 10 | 300W Xe Lamp (λ > 420 nm) | 2.3 | 1.0 | [44] |
| $SrTiO_3/TiO_2$ | 50 | Pt (0.3 wt%) | 150 | 300W Xe Lamp (λ > 420 nm) | 10.6 | 5.1 | [45] |
| $SrTiO_3$:Rh-RGO-$BiVO_4$:Mo | 200 | Ru (0.7 wt%) Co (0.1 wt%) | 120 | 300W Xe Lamp (λ > 420 nm) | 14 | 6.1 | [46] |
| Mg-doped $SrTiO_3$ | 25 | Ni (1 wt%) | 25 | 300W Xe Lamp (λ > 300 nm) | 8.8 | 4.2 | [47] |
| $PdCrO_x/SrTiO_3$ | 100 | / | 140 | 300W Xe Lamp (λ > 300 nm) | 15 | 5 | [48] |
| Ultrafine Pt clusters on $SrTiO_3$ | 50 | / | 100 | 300W Xe Lamp (λ > 300 nm) | 23 | 12 | [49] |
| $SrTiO_3$ (impregnation methods) | 300 | Pt (0.3 wt%) | 150 | 300W Xe Lamp (λ > 300 nm) | 38 | 20 | [50] |
| $TiO_2/SrTiO_3$ | 100 | Rh (0.1 wt%) Cr (0.05 wt%) Co (0.05 wt%) | 50 | 300W Xe Lamp (λ < 380 nm) | 38.6 | 19.2 | [51] |
| oxygen vacancies $SrTiO_3$ | 100 | Pt (0.3 wt%) | 60 | 300W Xe Lamp (λ < 380 nm) | 81 | 40 | [43] |

### *2.4. The Influence Factors of Enhancing Photocatalytic Performance*

The valence and conduction band structures are essential for the analysis of the underlying causes of the enhanced photocatalytic activity. As shown in Figure 5a, the UV-vis DRS of pure STO shows an absorption edge at 385 nm, consistent with the published literature [52]. Surprisingly, the GO/STO photocatalyst has a much higher absorption capacity for visible light compared to pure STO. Meanwhile, according to the equation $(\alpha h\upsilon) = A\ (h\upsilon - E_g)^{n/2}$, the plotting of $(\alpha h\upsilon)^{1/2}$ with respect to the energy ($h\upsilon$) is performed to calculate the band gap energy due to the indirect band gap ($n = 1$) property of STO [53], while the plotting of $(\alpha h\upsilon)^2$ with respect to the energy ($h\upsilon$) is performed due to the direct band gap ($n = 4$) property of GO/Rh-STO [33]. In Figure 5b, the band gap energies of STO and GO/Rh-STO are calculated to be 3.20 eV and 2.09 eV, respectively, which indicates that the combination of GO and STO greatly reduces the band gap energy and enhances the absorption and utilization of visible radiation. In addition, Mott–Schottky measurements were performed to investigate the conduction bands of STO and GO/Rh-STO. As shown in Figure 5c,d, the Mott–Schottky slopes of STO and GO/Rh-STO indicate a positive correlation, which indicates that they are all n-type semiconductors. The conduction band potentials of STO and GO/Rh-STO are −0.41 eV and −0.65 eV (vs. NHE), respectively, as calculated by the equation $E_{NHE} = E_{Ag/AgCl} + 0.059 \times PH + 0.197$. The VB potentials of STO and GO/Rh-STO were determined to be 2.79 eV and 1.44 eV from the empirical equation of $E_{VB} = E_{CB} + E_g$ [54,55].

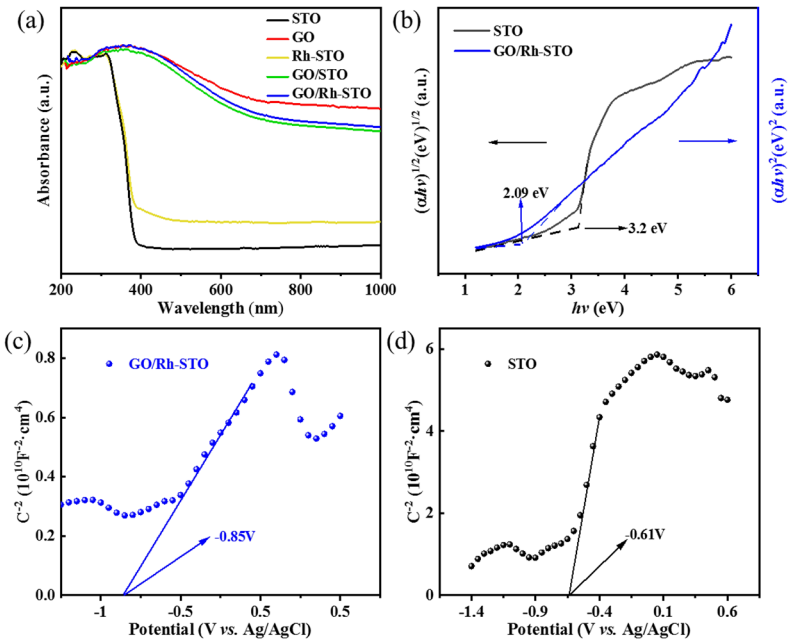


**Figure 5.** (**a**) UV−vis diffuse reflectance spectra and (**b**) curves of $(\alpha h\upsilon)^{1/2}$ and $(\alpha h\upsilon)^2$ versus energy ($h\upsilon$) of STO and GO/Rh−STO; Mott−Schottky curves of (**c**) GO/Rh−STO and (**d**) STO.

The photoelectric properties are closely related to the transfer and separation ability of the charge carriers of the photocatalyst. As shown in Figure 6a, the surface charge transfer efficiency of the samples was studied by EIS and the GO/Rh-STO samples show a much smaller semicircular diameter and much lower charge transfer resistance than pure STO. By calculating the diameter of the semicircle obtained by EIS, the charge transfer resistance ($R_{ct}$) of GO/STO, GO, and pure STO were 103.2, 41.3, and 279.5 Ω, respectively, and the conductivity ($R_{ct}^{-1}$) was from the largest to the smallest sample as GO>GO/STO>STO. This is also demonstrated by the linear sweep voltage plot (LSV) shown in Figure 6c, where the overpotential of GO/Rh-STO (1.19V) is smaller than that of pure STO (1.93 V) at $-10$ mA·cm$^{-2}$, indicating that the conductivity of GO/Rh-STO samples is better than that of STO. The improved electrical conductivity of GO/Rh-STO composites is due to the

introduction of GO with excellent electrical conductivity. Furthermore, Figure 6b shows the photocurrent responses of the prepared STO, GO, and GO/Rh-STO heterostructures, which all exhibit stable photocurrent signals over six cycles. Notably, the photocurrent intensity of the GO/Rh-STO samples is stronger than that of pure STO and GO, indicating that the GO/Rh-STO composites have better separation of charge–hole pairs.

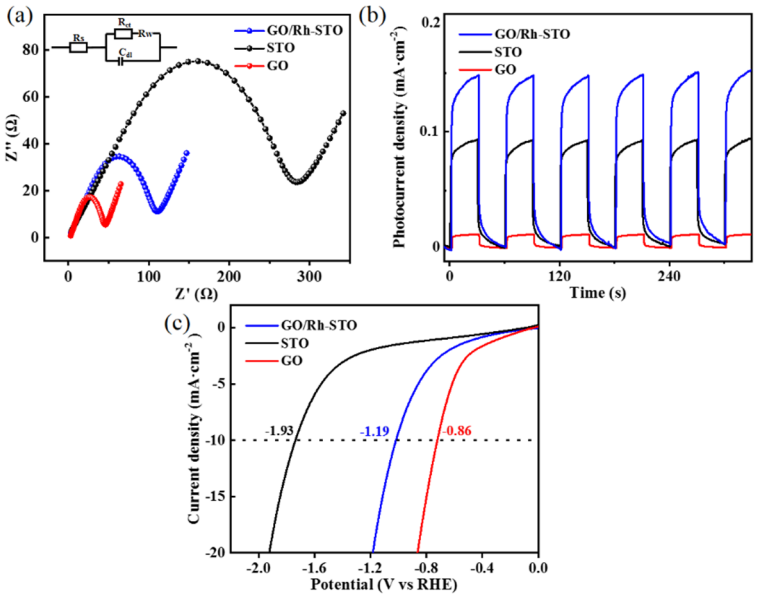


**Figure 6.** (**a**) EIS Nyquist plots, the electrical equivalent circuit model of as-prepared samples is shown in the inset of (a) including charge transfer resistance ($R_{ct}$), resistance of solution ($R_s$), double layer capacitance ($C_{dl}$) and Warburg resistance ($R_W$); (**b**) the transient photocurrent responses and; (**c**) LSV curves of STO, GO and GO/Rh−STO.

In this study of the behavior of charge separation of samples by photoluminescence (PL) and transient photoluminescence spectroscopy (TRPL), the PL spectra of photocatalysts at the excitation wavelength of 385 nm are depicted in Figure 7a, in which PL emission at 480 nm on as-prepared photocatalysts is shown. As shown in Figure 7b, under the condition of $\lambda_{ex}$ = 385 nm and $\lambda_{em}$ = 480 nm, we tracked the transient photoluminescence (TRPL) emission profile. From Figure 7b, the average decay lifetimes of GO/STO (1.6 ns) and GO/Rh-STO (1.9 ns) composite catalysts are longer compared to pure STO (1.1 ns), which further demonstrates the effective facilitative effect of the separation and transfer of photoinduced charges.

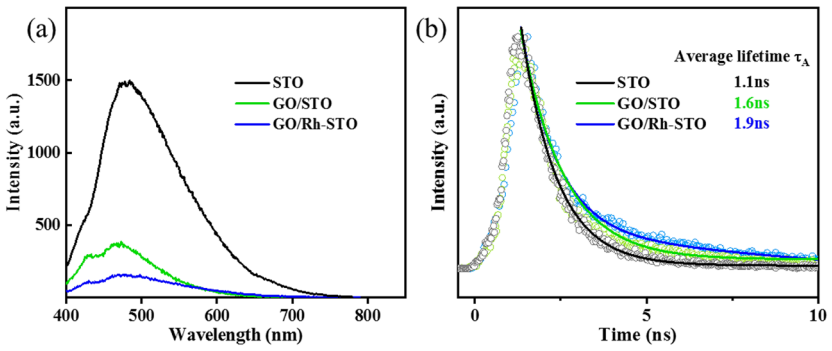


**Figure 7.** (**a**) PL spectra and (**b**) TRPL spectra of STO, GO/STO, and GO/Rh-STO ($\lambda_{ex}$ = 385 nm and $\lambda_{em}$ = 480 nm).

Furthermore, the specific surface area was investigated in order to investigate the factors affecting the activity of photocatalytic water splitting. As is shown in Figure 8a–c,

the $N_2$ adsorption–desorption isotherms show that the samples GO, STO, and GO/Rh-STO all exhibit typical type IV isotherms with H3-type hysteresis loops. This indicates the existence of multi-porous structures in GO, STO, and GO/Rh-STO. The BET surface area of the GO/Rh-STO (22.537 $m^2/g$, Figure 8a) composites was significantly larger compared to that of STO (4.15 $m^2/g$, Figure 8c), which was mainly attributed to the large specific surface area of GO. In addition, the composition of GO/Rh-STO nanocomposites was analyzed by Raman spectroscopy. As shown in Figure 8d, STO has secondary Raman scattering from 160 $cm^{-1}$ to 451 $cm^{-1}$, which leads to a continuous broadband. STO shows its characteristic peaks at 171, 245, 307, 609, 674, and 1044 $cm^{-1}$ [56,57] and GO shows its characteristic peaks at 1393 $cm^{-1}$ (D-band) and 1596 $cm^{-1}$ (G-band). Two additional bands of GO/Rh-STO were obtained at 1392 (D-band) and 1595 $cm^{-1}$ (G-band) [58], which confirmed the presence of GO. Therefore, the Raman spectra illustrate the successful preparation of GO/Rh-STO nanocomposites.

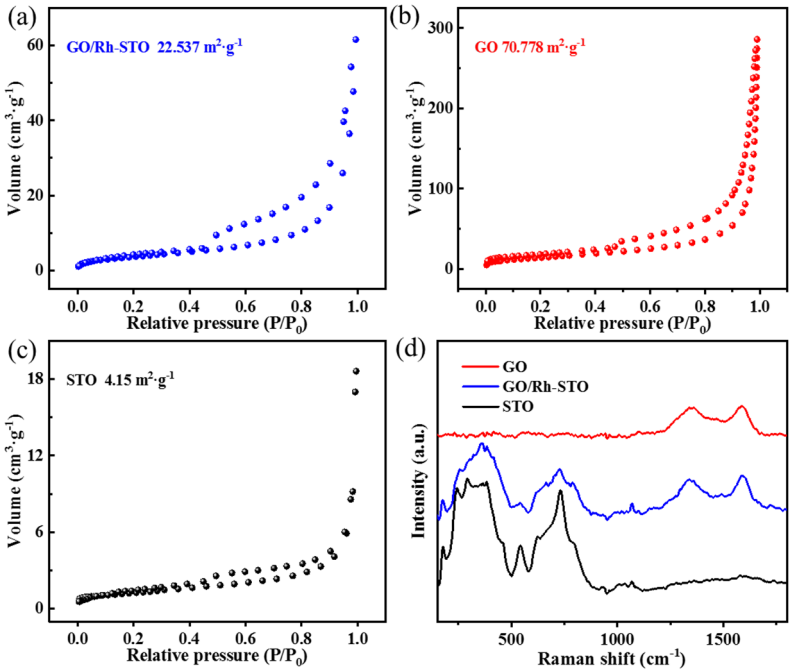


**Figure 8.** Nitrogen adsorption–desorption curves of (**a**) GO/Rh−STO, (**b**) GO, (**c**) STO, and (**d**) Raman spectra of GO, STO, and GO/Rh−STO.

### *2.5. Photocatalytic Mechanism Research*

Based on the above experimental results, the mechanism of the photocatalytic reaction on GO/Rh-STO heterostructure is shown in Figure 9. According to the above study, the VB and CB energy levels of STO were confirmed to be 2.79 eV and −0.41 eV, respectively. The Fermi energy level of GO is −0.008 V with respect to NHE [59]. The CB energy level of STO is −0.41 eV, which is positive for the Fermi energy level of GO. As a result, the photoexcited electrons are rapidly transferred from the CB of STO to GO, thereby suppressing the photoexcited $e^-/h^+$ pairs' recombination and improving their separation efficiency. During the photocatalytic experiments, when the light starts being exposed on the photocatalyst, STO absorbs the light and the $e^-$ production of STO transfers from VB to CB and the $h^+$ were left at VB of STO. Due to the solid-solid tight contact interface, GO facilitates the rapid transfer of $e^-$ to the Rh active sites. The $e^-$ transfers quickly to the Rh active sites and produces $H_2$ with $H^+$. Meanwhile, $h^+$ on the VB of STO produces $O_2$ with water, because the valence band maximum for the STO is located at a more positive position than the $O_2/H_2O$ energy level [60].

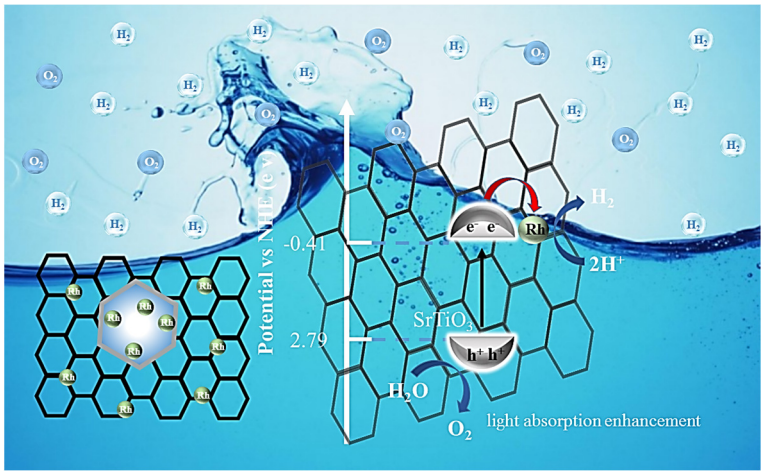


**Figure 9.** Schematic representation of possible photocatalytic degradation mechanism.

## 3. Experiment

### *3.1. Materials*

Titanium butoxide ($C_{16}H_{36}O_4Ti$), sodium hydroxide (NaOH), strontium chloride ($SrCl_2$), rhodium(III) chloride trihydrate ($RhCl_3{\cdot}3H_2O$), and graphite powder were obtained from Shanghai Aladdin Technology Co., Ltd. (Shanghai, China). Ethanol ($C_2H_5OH$), hydrochloric acid (HCl), sulphuric acid ($H_2SO_4$), hydrogen peroxide solution ($H_2O_2$), sodium nitrate ($NaNO_3$), and potassium permanganate ($KMnO_4$) were obtained from Shanghai Sinopharm Co., Ltd. (Shanghai, China). All reagents involved in the experiments were of analytical grade (purity $\geq$ 99.0%) and the water used throughout the study was deionized water (DI).

### *3.2. Synthesis and Preparation*

#### 3.2.1. Synthesis of Graphene Oxide (GO)

GO was synthesized using a modified Hummer method which is reported in the other literature [61]. In short, 100 mL $H_2SO_4$ (98%) was added to a round-bottom flask (500 mL) in an ice bath with stirring at 450 rpm. Graphite powder (5 g), $NaNO_3$ (1.6 g), and $KMnO_4$ (10 g) were added to concentrated sulfuric acid. An amount of 100 mL $H_2O$ was added to the mixture when the color of the reaction mixture turned light gray. After increasing the temperature of the reaction vessel to 102 °C for 2 h, $H_2O_2$ (40 mL) was added. The reaction mixture was washed with 5% HCl until the filtrate became colorless after stirring the reaction mixture for 1 h. Then, we obtained graphite oxide after washing 3 times with $H_2O$ and dried it in a desiccator at 60 °C. Finally, we obtained GO by ultrasonication of the dispersed graphite oxide in water.

#### 3.2.2. Synthesis of Strontium Titanate (STO)

The STO nanoparticle was synthesized via a hydrothermal route [62]. Firstly, $SrCl_2$ (0.01 mol) was added to an autoclave (50 mL) followed by 30 mL of water. After stirring for 20 min, 3.4 mL titanium butoxide was added, then 0.8 g NaOH. After stirring for 2 h, the autoclave was heated to 195 °C and held for 23 h. After the completion of the reaction, the reaction was washed by centrifugation several times and dried at 60 °C. Finally, we obtained STO white powder.

#### 3.2.3. Synthesis of GO/Rh-STO Composite Catalysts

GO/Rh-STO composites were synthesized by the hydrothermal method [63]. Firstly, $SrCl_2$ (0.01 mol) and $RhCl_3{\cdot}3H_2O$ (50 mg) were added to an autoclave (50 mL) followed by 30 mL of water. After stirring for 20 min, 3.4 mL titanium butoxide was added, then 0.8 g NaOH. After stirring for 30 min, 20 mg GO was added. After stirring for 2 h, the autoclave was heated to 195 °C and held for 23 h. After the completion of the reaction, the reaction

was washed by centrifugation several times and dried at 60 °C to obtain GO/Rh-STO precursor powder. Finally, we obtained the GO/Rh-STO composite catalysts by annealing at 200 °C in ambient for 2 h. The xGO/Rh-STO composites were synthesized by changing the amount of GO (10 mg, 20 mg, 40 mg, 60 mg). The percentages of C atomic were 3.8%, 7.2%, 12.2%, and 16.9%, which named 3.8% GO/Rh-STO, 7.2% GO/Rh-STO, 12.2% GO/Rh-STO, and 16.9% GO/Rh-STO, respectively, according to the C atomic percentage analysis of XPS in Table 1.

### *3.3. Evaluation on Efficiency of Photocatalysts*

The evaluation of the overall water splitting performance was performed on a CEL-PAEM-D8 photocatalytic activity evaluation system (CEL-PF300-T9) equipped with a 300W xenon lamp (Beijing Zhongjiao Jinyuan Technology Co., Ltd., Beijing, China) and a cutoff filter allowing $\lambda > 420$ nm. Briefly, 0.1 g of catalyst was dispersed in an light reactor containing 100 mL of water, connected to the photoreaction system, and then evacuated. The reactor was irradiated with a 300w xenon lamp as the light source for performance testing. The produced $H_2$ and $O_2$ were evaluated hourly on a gas chromatograph (GC 7920) using high-purity Ar as the carrier gas, and the amounts of $H_2$ and $O_2$ were calculated from their standard curves.

### *3.4. Characterization*

The structure and crystalline phase of the samples were analyzed by XPS (Thermo Fisher Scientific K-Alpha, Waltham, MA, USA) and XRD (Rigaku Ultima IV, Tokyo, Japan). X-ray photoelectron spectroscopy (XPS) analysis was conducted on a Thermo Fisher Scientific K-Alpha photoelectron spectroscopy at $5.0 \times 10^{-10}$ mbar. X-ray diffraction (XRD) patterns of the samples were collected with a scan rate of 0.02°. The morphology was observed on a field emission scanning electron microscope (Hitachi Regulus 8100, Tokyo, Japan) and a field emission transmission electron microscope (FEI Talos F200X G2, Waltham, MA, USA). Transmission electron microscopy (TEM) and high-resolution TEM (HRTEM) images were obtained by an FEI Talos F200X G2 instrument at an accelerating voltage of 200 kV. The diffuse reflectance UV-visible (DRS) was recorded with a PE Lambda 750. The specific surface area was analyzed on an $N_2$ adsorption–desorption device (TriStar II 20, Waltham, MA, USA) at 77 K, and the samples were degassed at 120 °C for 6 h in a vacuum before the measurements were taken. The photoluminescence (PL) spectra and transient photoluminescence spectra (TRPL) were measured using an Edinburgh FLS-1000 spectrofluorometer.

### *3.5. Electrochemical Tests*

The electrochemical properties of the samples were tested on a CHI600E electrochemical workstation. The platinum electrode, ITO glass (1 cm × 2 cm) coated by sample, and $Ag^+/AgCl$ electrode served as counter electrode, working electrode, and reference electrode to build the three-electrode system in 0.5 M $H_2SO_4$ electrolyte.

## 4. Conclusions

In conclusion, we reported a GO/Rh-$SrTiO_3$ composite that was prepared by a simple hydrothermal process for overall water splitting. The champion catalyst realized $H_2$ production rate of 55.83 $\mu mol \cdot g^{-1} \cdot h^{-1}$ and $O_2$ production rate of 23.26 $\mu mol \cdot g^{-1} \cdot h^{-1}$ under visible light ($\lambda \geq 420$ nm). The studies of microstructure, physicochemical properties, and photoelectric behavior demonstrated that the GO/Rh-$SrTiO_3$ heterojunction can work under visible light, which greatly improves the utilization of sunlight. Moreover, the Rh metal as the electron acceptor, which greatly increases the active sites and promotes the electron–hole separation and transfer. This work provides a new strategy to transform traditional UV catalysts into visible-light-responsive catalysts with abundant active sites.

**Author Contributions:** Conceptualization, P.H. and Y.Y. (Yongsheng Yan); methodology, Y.Y. (Yan Yan); software, E.J.; validation, S.Z., J.W. and Z.L.; formal analysis, Y.Y. (Yan Yan); investigation, S.Z.; resources, Y.Y. (Yongsheng Yan); data curation, S.Z.; writing—original draft preparation, S.Z.; writing—review and editing, E.J.; visualization, S.Z.; supervision, J.W.; project administration, Y.Y. (Yan Yan); funding acquisition, Y.Y. (Yongsheng Yan). All authors have read and agreed to the published version of the manuscript.

**Funding:** This research was funded by the National Natural Science Foundation of China (Grant No. 21776117 and 21806060).

**Data Availability Statement:** Not applicable.

**Conflicts of Interest:** The authors declare no competing financial interest.

## References

1. Wang, W.; Xu, M.; Xu, X.; Zhou, W.; Shao, Z. Perovskite oxide based electrodes for high-performance photoelectrochemical water splitting. *Angew. Chem. Int. Ed.* **2020**, *59*, 136–152. [CrossRef] [PubMed]
2. Niu, W.; Yang, Y. Graphitic carbon nitride for electrochemical energy conversion and storage. *ACS Energy Lett.* **2018**, *3*, 2796–2815. [CrossRef]
3. Zhou, Z.; Pei, Z.; Wei, L.; Zhao, S.; Jian, X.; Chen, Y. Electrocatalytic hydrogen evolution under neutral pH conditions: Current understandings, recent advances, and future prospects. *Energy Environ. Sci.* **2020**, *13*, 3185–3206. [CrossRef]
4. Holladay, J.D.; Hu, J.; King, D.L.; Wang, Y. An overview of hydrogen production technologies. *Catal. Today* **2009**, *139*, 244–260. [CrossRef]
5. LeValley, T.L.; Richard, A.R.; Fan, M. The progress in water gas shift and steam reforming hydrogen production technologies—A review. *Int. J. Hydrogen Energy* **2014**, *39*, 16983–17000. [CrossRef]
6. Hisatomi, T.; Kubota, J.; Domen, K. Recent advances in semiconductors for photocatalytic and photoelectrochemical water splitting. *Chem. Soc. Rev.* **2014**, *43*, 7520–7535. [CrossRef] [PubMed]
7. Jiang, R.; Lu, G.; Yan, Z.; Wu, D.; Zhou, R.; Bao, X. Insights into a CQD-$SnNb_2O_6$/BiOCl Z-scheme system for the degradation of benzocaine: Influence factors, intermediate toxicity and photocatalytic mechanism. *Chem. Eng. J.* **2019**, *374*, 79–90. [CrossRef]
8. Che, H.; Che, G.; Zhou, P.; Liu, C.; Dong, H.; Li, C.; Li, C. Nitrogen doped carbon ribbons modified g-$C_3N_4$ for markedly enhanced photocatalytic $H_2$-production in visible to near-infrared region. *Chem. Eng. J.* **2020**, *382*, 122870. [CrossRef]
9. Tang, M.; Ao, Y.; Wang, C.; Wang, P. Rationally constructing of a novel dual Z-scheme composite photocatalyst with significantly enhanced performance for neonicotinoid degradation under visible light irradiation. *Appl. Catal. B Environ.* **2020**, *270*, 118918. [CrossRef]
10. Li, C.; Yu, S.; Zhang, X.; Wang, Y.; Liu, C.; Chen, G.; Dong, H. Insight into photocatalytic activity, universality and mechanism of copper/chlorine surface dual-doped graphitic carbon nitride for degrading various organic pollutants in water. *J. Colloid Interface Sci.* **2019**, *538*, 462–473. [CrossRef]
11. Patial, S.; Hasija, V.; Raizada, P.; Singh, P.; Singh, A.A.P.K.; Asiri, A.M. Tunable photocatalytic activity of $SrTiO_3$ for water splitting: Strategies and future scenario. *J. Environ. Chem. Eng.* **2020**, *8*, 103791. [CrossRef]
12. Szafraniak, B.; Fusnik, Ł.; Xu, J.; Gao, F.; Brudnik, A.; Ry-dosz, A. Semiconducting metal oxides: $SrTiO_3$, $BaTiO_3$ and $BaSrTiO_3$ in gas-sensing applications: A review. *Coatings* **2021**, *11*, 185. [CrossRef]
13. Jayabal, P.; Sasirekha, V.; Mayandi, J.; Jeganathan, K.; Ramakrishnan, V. A facile hydrothermal synthesis of $SrTiO_3$ for dye sensitized solar cell application. *J. Alloys Compd.* **2014**, *586*, 456–461. [CrossRef]
14. Ghosh, D.; Giri, S.; Sahoo, S.; Das, C.K. In situ synthesis of graphene/amine-modified graphene, polypyrrole composites in presence of $SrTiO_3$ for supercapacitor applications. *Polym. Plast. Technol. Eng.* **2013**, *52*, 213–220. [CrossRef]
15. Muhamad, N.F.; Osman, R.A.M.; Idris, M.S.; Yasin, M.N.M. Physical and electrical properties of $SrTiO_3$ and $SrZrO_3$//EPJ Web of Conferences. *EDP Sci.* **2017**, *162*, 01052.
16. Hu, X.J.; Yang, Y.; Hou, C.; Liang, T.X. Thermodynamic and Electronic Properties of Two-Dimensional $SrTiO_3$. *J. Phys. Chem. C* **2021**, *126*, 517–524. [CrossRef]
17. Liu, G.; Zhao, Y.; Sun, C.; Li, F.; Lu, G.Q.; Cheng, H.M. Synergistic effects of B/N doping on the visible-light photocatalytic activity of mesoporous $TiO_2$. *Angew. Chem. Int. Ed.* **2008**, *47*, 4516–4520. [CrossRef]
18. Zhang, X.; Wang, Y.; Liu, B.; Sang, Y.; Liu, H. Heterostructures construction on $TiO_2$ nanobelts: A powerful tool for building high-performance photocatalysts. *Appl. Catal. B Environ.* **2017**, *202*, 620–641. [CrossRef]
19. Zhang, Z.; Huang, L.; Zhang, J.; Wang, F.; Xie, Y.; Shang, X.; Wang, X. In situ constructing interfacial contact $MoS_2/ZnIn_2S_4$ heterostructure for enhancing solar photocatalytic hydrogen evolution. *Appl. Catal. B Environ.* **2018**, *233*, 112–119. [CrossRef]
20. Maarisetty, D.; Baral, S.S. Defect engineering in photocatalysis: Formation, chemistry, optoelectronics, and interface studies. *J. Mater. Chem. A* **2020**, *8*, 18560–18604. [CrossRef]
21. Bai, S.; Zhang, N.; Gao, C.; Xiong, Y. Defect engineering in photocatalytic materials. *Nano Energy* **2018**, *53*, 296–336. [CrossRef]
22. Putri, L.K.; Ong, W.J.; Chang, W.S.; Chai, S.P. Heteroatom doped graphene in photocatalysis: A review. *Appl. Surf. Sci.* **2015**, *358*, 2–14. [CrossRef]

23. Cui, D.; Hao, W.; Chen, J. The synergistic effect of heteroatom doping and vacancy on the reduction of $CO_2$ by photocatalysts. *ChemNanoMat* **2021**, *7*, 894–901. [CrossRef]
24. Zhang, L.H.; Shi, Y.; Wang, Y.; Shiju, N.R. Nanocarbon catalysts: Recent understanding regarding the active sites. *Adv. Sci.* **2020**, *7*, 1902126. [CrossRef] [PubMed]
25. Li, Y.; Li, X.; Zhang, H.; Fan, J.; Xiang, Q. Design and application of active sites in g-$C_3N_4$-based photocatalysts. *J. Mater. Sci. Technol.* **2020**, *56*, 69–88. [CrossRef]
26. Ha, M.N.; Zhu, F.; Liu, Z.; Wang, L.; Liu, L.; Lu, G.; Zhao, Z. Morphology-controlled synthesis of $SrTiO_3/TiO_2$ heterostructures and their photocatalytic performance for water splitting. *RSC Adv.* **2016**, *6*, 21111–21118. [CrossRef]
27. Deng, Y.; Shu, S.; Fang, N.; Wang, R.; Chu, Y.; Liu, Z.; Cen, W. One-pot synthesis of $SrTiO_3$-$SrCO_3$ heterojunction with strong interfacial electronic interaction as a novel photocatalyst for water splitting to generate $H_2$. *Chin. Chem. Lett.* **2023**, *34*, 107323. [CrossRef]
28. Pan, J.H.; Shen, C.; Ivanova, I.; Zhou, N.; Wang, X.; Tan, W.C.; Wang, Q. Self-template synthesis of porous perovskite titanate solid and hollow submicrospheres for photocatalytic oxygen evolution and mesoscopic solar cells. *ACS Appl. Mater. Interfaces* **2015**, *7*, 14859–14869. [CrossRef]
29. Xiang, Q.; Yu, J.; Jaroniec, M. Graphene-based semiconductor photocatalysts. *Chem. Soc. Rev.* **2012**, *41*, 782–796. [CrossRef]
30. Zhang, N.; Zhang, Y.; Xu, Y.J. Recent progress on graphene-based photocatalysts: Current status and future perspectives. *Nanoscale* **2012**, *4*, 5792–5813. [CrossRef]
31. Johra, F.T.; Jung, W.G. RGO–$TiO_2$–ZnO composites: Synthesis, characterization, and application to photocatalysis. *Appl. Catal. A Gen.* **2015**, *491*, 52–57. [CrossRef]
32. Gao, P.; Liu, J.; Sun, D.D.; Ng, W. Graphene oxide–CdS composite with high photocatalytic degradation and disinfection activities under visible light irradiation. *J. Hazard. Mater.* **2013**, *250*, 412–420. [CrossRef] [PubMed]
33. Hunge, Y.M.; Yadav, A.A.; Dhodamani, A.G.; Suzuki, N.; Terashima, C.; Fujishima, A.; Mathe, V.L. Enhanced photocatalytic performance of ultrasound treated GO/$TiO_2$ composite for photocatalytic degradation of salicylic acid under sunlight illumination. *Ultrason. Sonochem.* **2020**, *61*, 104849. [CrossRef] [PubMed]
34. Wang, Y.; Du, Y.; Fu, Z.; Ren, J.; Fu, Y.; Wang, L. Construction of Ru/FeCoP heterointerface to drive dual active site mechanism for efficient overall water splitting. *J. Mater. Chem. A* **2022**, *10*, 16071–16079. [CrossRef]
35. Shahabuddin, S.; Muhamad Sarih, N.; Mohamad, S.; Joon Ching, J. $SrTiO_3$ nanocube-doped polyaniline nanocomposites with enhanced photocatalytic degradation of methylene blue under visible light. *Polymers* **2016**, *8*, 27. [CrossRef]
36. Zhang, K.; Zhang, L.L.; Zhao, X.S.; Wu, J. Graphene/polyaniline nanofiber composites as supercapacitor electrodes. *Chem. Mater.* **2010**, *22*, 1392–1401. [CrossRef]
37. Kumar, N.A.; Choi, H.J.; Shin, Y.R.; Chang, D.W.; Dai, L.; Baek, J.B. Polyaniline-grafted reduced graphene oxide for efficient electrochemical supercapacitors. *ACS Nano* **2012**, *6*, 1715–1723. [CrossRef]
38. Kiss, B.; Manning, T.D.; Hesp, D.; Didier, C.; Taylor, A.; Pickup, D.M.; Rosseinsky, M.J. Nano-structured rhodium doped $SrTiO_3$–Visible light activated photocatalyst for water decontamination. *Appl. Catal. B Environ.* **2017**, *206*, 547–555. [CrossRef]
39. Kawasaki, S.; Nakatsuji, K.; Yoshinobu, J.; Komori, F.; Takahashi, R.; Lippmaa, M.; Kudo, A. Epitaxial Rh-doped $SrTiO_3$ thin film photocathode for water splitting under visible light irradiation. *Appl. Phys. Lett.* **2012**, *101*, 033910. [CrossRef]
40. Kiran, K.S.; Ashwath Narayana, B.S.; Lokesh, S.V. Enhanced photocatalytic activity of perovskite $SrTiO_3$ nanorods. *Solid State Technol.* **2020**, *63*, 1913–1920.
41. Zhao, W.; Wang, H.; Liu, N.; Rong, J.; Zhang, Q.; Li, M.; Yang, X. Hydrothermal synthesis of Litchi-like $SrTiO_3$ with the help of ethylene glycol. *J. Am. Ceram. Soc.* **2019**, *102*, 981–987. [CrossRef]
42. Yang, D.; Sun, Y.; Tong, Z.; Nan, Y.; Jiang, Z. Fabrication of bimodal-pore $SrTiO_3$ microspheres with excellent photocatalytic performance for Cr (VI) reduction under simulated sunlight. *J. Hazard. Mater.* **2016**, *312*, 45–54. [CrossRef] [PubMed]
43. Kong, C.; Su, X.; Qing, D.; Zhao, Y.; Wang, J.; Zeng, X. Controlled synthesis of various $SrTiO_3$ morphologies and their effects on photoelectrochemical cathodic protection performance. *Ceram. Int.* **2022**, *48*, 20228–20236. [CrossRef]
44. Fan, Y.; Liu, Y.; Cui, H.; Wang, W.; Shang, Q.; Shi, X.; Tang, B. Photocatalytic overall water splitting by $SrTiO_3$ with surface oxygen vacancies. *Nanomaterials* **2020**, *10*, 2572. [CrossRef] [PubMed]
45. Wei, Y.; Wang, J.; Yu, R.; Wan, J.; Wang, D. Constructing $SrTiO_3$–$TiO_2$ heterogeneous hollow multi-shelled structures for enhanced solar water splitting. *Angew. Chem. Int. Ed.* **2019**, *58*, 1422–1426. [CrossRef]
46. Iwase, A.; Udagawa, Y.; Yoshino, S.; Ng, Y.H.; Amal, R.; Kudo, A. Solar Water Splitting under Neutral Conditions Using Z-Scheme Systems with Mo-Doped $BiVO_4$ as an $O_2$-Evolving Photocatalyst. *Energy Technol.* **2019**, *7*, 1900358. [CrossRef]
47. Han, K.; Lin, Y.C.; Yang, C.M.; Jong, R.; Mul, G.; Mei, B. Promoting photocatalytic overall water splitting by controlled magnesium incorporation in $SrTiO_3$ photocatalysts. *ChemSusChem* **2017**, *10*, 4510–4516. [CrossRef]
48. Kanazawa, T.; Nozawa, S.; Lu, D.; Maeda, K. Structure and photocatalytic activity of $PdCrO_x$ cocatalyst on $SrTiO_3$ for overall water splitting. *Catalysts* **2019**, *9*, 59. [CrossRef]
49. Qureshi, M.; Garcia-Esparza, A.T.; Jeantelot, G.; Ould-Chikh, S.; Aguilar-Tapia, A.; Hazemann, J.L.; Takanabe, K. Catalytic consequences of ultrafine Pt clusters supported on $SrTiO_3$ for photocatalytic overall water splitting. *J. Catal.* **2019**, *376*, 180–190. [CrossRef]
50. Zhang, X.; Li, Z.; Liu, T.; Li, M.; Zeng, C.; Matsumoto, H.; Han, H. Water oxidation sites located at the interface of Pt/$SrTiO_3$ for photocatalytic overall water splitting. *Chin. J. Catal.* **2022**, *43*, 2223–2230. [CrossRef]

51. Zhuo, Z.; Wang, X.; Shen, C.; Cai, M.; Jiang, Y.; Xue, Z.; Sun, S. Construction of $TiO_2/SrTiO_3$ Heterojunction Derived from Monolayer $Ti_3C_2$ MXene for Efficient Photocatalytic Overall Water Splitting. *Chem. A Eur. J.* **2023**, *29*, e202203450. [CrossRef] [PubMed]
52. Liu, J.W.; Chen, G.; Li, Z.H.; Zhang, Z.G. Electronic structure and visible light photocatalysis water splitting property of chromium-doped $SrTiO_3$. *J. Solid State Chem.* **2006**, *179*, 3704–3708. [CrossRef]
53. Ouyang, S.; Tong, H.; Umezawa, N.; Cao, J.; Li, P.; Bi, Y.; Ye, J. Surface-alkalinization-induced enhancement of photocatalytic $H_2$ evolution over $SrTiO_3$-based photocatalysts. *J. Am. Chem. Soc.* **2012**, *134*, 1974–1977. [CrossRef] [PubMed]
54. Zhao, Y.; Wang, Y.; Liang, X.; Shi, H.; Wang, C.; Fan, J.; Liu, E. Enhanced photocatalytic activity of Ag-$CsPbBr_3$/CN composite for broad spectrum photocatalytic degradation of cephalosporin antibiotics 7-ACA. *Appl. Catal. B Environ.* **2019**, *247*, 57–69. [CrossRef]
55. Xu, B.; Li, Y.; Gao, Y.; Liu, S.; Lv, D.; Zhao, S.; Ge, L. Ag-AgI/$Bi_3O_4Cl$ for efficient visible light photocatalytic degradation of methyl orange: The surface plasmon resonance effect of Ag and mechanism insight. *Appl. Catal. B Environ.* **2019**, *246*, 140–148. [CrossRef]
56. Yu-Lei, D.; Guang, C.; Ming-Sheng, Z.; Sen-Zu, Y. Phonon characteristics of polycrystalline cubic $SrTiO_3$ thin films. *Chin. Phys. Lett.* **2003**, *20*, 1561. [CrossRef]
57. Rahman, J.U.; Du, N.V.; Nam, W.H.; Shin, W.H.; Lee, K.H.; Seo, W.S.; Lee, S. Grain boundary interfaces controlled by reduced graphene oxide in nonstoichiometric $SrTiO_3$-δ thermoelectrics. *Sci. Rep.* **2019**, *9*, 8624. [CrossRef]
58. Kogularasu, S.; Govindasamy, M.; Chen, S.M.; Akilarasan, M.; Mani, V. 3D graphene oxide-cobalt oxide polyhedrons for highly sensitive non-enzymatic electrochemical determination of hydrogen peroxide. *Sens. Actuators B Chem.* **2017**, *253*, 773–783. [CrossRef]
59. Huang, C.; Li, C.; Shi, G. Graphene based catalysts. *Energy Environ. Sci.* **2012**, *5*, 8848–8868. [CrossRef]
60. Chen, S.; Takata, T.; Domen, K. Particulate photocatalysts for overall water splitting. *Nat. Rev. Mater.* **2017**, *2*, 17050. [CrossRef]
61. Wang, X.; Dou, W. Preparation of graphite oxide (GO) and the thermal stability of silicone rubber/GO nanocomposites. *Thermochim. Acta* **2012**, *529*, 25–28. [CrossRef]
62. Wei, X.; Xu, G.; Ren, Z.; Xu, C.; Weng, W.; Shen, G.; Han, G. Single-Crystal-like Mesoporous $SrTiO_3$ Spheres with Enhanced Photocatalytic Performance. *J. Am. Ceram. Soc.* **2010**, *93*, 1297–1305.
63. Wei, X.; Xu, G.; Ren, Z.; Xu, C.; Shen, G.; Han, G. PVA-Assisted Hydrothermal Synthesis of $SrTiO_3$ Nanoparticles with Enhanced Photocatalytic Activity for Degradation of RhB. *J. Am. Ceram. Soc.* **2008**, *91*, 3795–3799. [CrossRef]